Surface & Coatings Technology 335 (2018) 41–51

Contents lists available at ScienceDirect

Surface & Coatings Technology

journal homepage: www.elsevier.com/locate/surfcoat

Microstructure and lifetime of Hf or Zr doped sputtered NiAlCr bond coat/7YSZ EB-PVD TBC systems

J. Muñoz Saldaña[a,b,*,1], U. Schulz[a], G.C. Mondragón Rodríguez[a,c], L.A. Caceres-Diaz[b], H. Lau[a,2]

[a] German Aerospace Center (DLR), Institute of Materials Research, Cologne, Germany
[b] Centro de Investigación y de Estudios Avanzados del IPN, Lib. Norponiente 2000, Fracc. Real de Juriquilla, 76230 Querétaro, Qro., Mexico
[c] Center of Engineering and Industrial Development, CIDESI, Av. Pie de la Cuesta No. 702, 76125 Querétaro, Qro., Mexico

ARTICLE INFO

Keywords:
Thermal barrier coating
Sputtering
Bond coats
Furnace cyclic tests

ABSTRACT

NiAlCr-X overlay coatings deposited by magnetron sputtering on IN100 and CMSX-4 superalloys and thereafter top-coated with 7YSZ thermal barrier coatings by EB-PVD were investigated with emphasis on the effects of superalloy type and Hf or Zr doping. The sputtered films in the "as coated" condition (after EB-PVD deposition) showed strong diffusion effects of different elements from the superalloys. The measured phase content of β and γ′ was in good agreement with calculated data obtained from experimental compositions normalized to a Ni-Al-Cr system following the guidelines of site preference of ternary alloying elements. Microstructure evolution and failure characteristics after furnace cyclic tests at 1100 °C were investigated as well. The lifetime of the coatings is equivalent to standard MCrAlY TBCs systems and is compared to PtAl and NiCoCrAlY coatings from literature. The effects of microstructure and elements diffusing from the substrates into the bond coat (Ti, Co, Mo and Ta) in combination with the effect of Hf- or Zr-doping is presented and discussed.

1. Introduction

Thermal barrier coatings (TBCs) are protective systems that promote more efficient gas turbine engines and prolonged lifetime of metallic components [1,2]. TBC's contain different layers on a Ni-based superalloy such as a bond coat (BC), typically a Ni-base alloy that serves as the Al-reservoir to form a thermally grown oxide (TGO) of α-Al_2O_3, which is structurally compatible with the insulating top coat (TC) (commonly 7–8 wt% Y_2O_3 doped ZrO_2 denominated as 7YSZ) [1–5].

It is well known that the TBC layers are affected by a number of factors when operating at high temperatures. In bond coats the dominant effect is the variation in Al content due to oxidation and diffusion into the substrate. Other effects include the diffusion of elements from the superalloy into the BC during operation or under cyclic loading. The combination of these affects the microstructure and chemical properties of the BC leading to the activation of intrinsic failure mechanisms such as spallation of the TBC and rumpling of the BC [3,6–8]. In the case of 7YSZ deposited by electron beam-physical vapor deposition, TBC failure is almost always initiated near to the TGO, mostly along the TGO/BC or TGO/TC interface [4,9,10].

Although many efforts have been undertaken to understand the complex phenomena occurring in the layers and interfaces of TBC systems and their effects on TBC performance in furnace cyclic tests (FCT) and in service, there are still a number of microstructural effects that are not fully understood in detail. Among others, these effects include phase transformations due to Al-depletion based on bi-directional Al-diffusion (outward or inward), internal cracks/oxidation, Kirkendall pores, martensitic transformation during heating and cooling, diffusion of substrate elements leading to the formation of an interdiffusion zone (IDZ) containing topological close-packed (TCP) phases, etc.

The FCT is frequently used to get a standardized lifetime for TBCs, exposing them for defined periods between high and room temperatures. Typically, the specimens are cycled in 1 h intervals including heating and cooling steps. Forced air cooling is added to increase the severity of the thermal shock on the specimens. One of the most important parameters defining the furnace cyclic life is the top temperature, where a life reduction of ~90% for every 100 °C increase is observed [11].

The composition of the superalloy and the inter-diffusion effects with the BC play as well a decisive role for TBC life time, especially in EB-PVD TBC systems [12–16].

From all the modifying elements in bond coats, the particular

* Corresponding author at: Centro de Investigación y de Estudios Avanzados del IPN, Lib. Norponiente 2000, Fracc. Real de Juriquilla, 76230 Querétaro, Qro., Mexico.
E-mail address: jmunoz@cinvestav.mx (J. Muñoz Saldaña).

[1] **Georg Forster** Humboldt fellow.

[2] Now at Lloyd's Register EMEA, Adolf-Grimme-Allee 3, 50829 Cologne, Germany.

https://doi.org/10.1016/j.surfcoat.2017.12.017
Received 16 February 2017; Received in revised form 6 December 2017; Accepted 7 December 2017
Available online 12 December 2017
0257-8972/

positive effects of Cr additions for fracture toughness, strength, and ductility of NiAl as a function of temperature have been experimentally addressed [17,18]. Cr accelerates the Al_2O_3 theta to alpha phase transformation and is a key component in the reduction of hot corrosion attack of NiAl alloys [13,16,19–22].

The particular effect of reactive elements (RE) such as Hf, La, Zr, Dy, Ce or Y [17–20,23–34] in NiAl as well as combined additions of Cr + Hf or Cr + Zr, Hf + Zr or Hf + Ru have been previously reported [19,24,35,36]. It is generally agreed that doping of these alloys in the right amounts of RE has a positive effect on TBC life-time by improving the alumina scale adhesion, growth mechanism, and thus the oxidation resistance of the whole system [25,29,36–40]. The RE effect has been explained by the so called dynamic segregation theory [30]. The oxygen active elements diffuse outward due to the oxygen potential gradient and segregate to the metal-oxide interface and to alumina grain boundaries in the TGO where they block the cations movement, thus inhibiting the outward diffusion of Al^{3+} cations. As a result, the alumina scale grows predominantly by inward transport of O^{2-} anions, mainly along the scale grain boundaries. This is strongly diminished when the temperature is high enough to stabilize the α-Al_2O_3 phase. Hf-containing bond coats or superalloys frequently deliver the longest TBC life times. An optimum content of the RE elements (Hf, Zr or Y) for improved oxidation behavior of NiAl coatings (without TBC) has been consistently identified, which seems to be affected by the type of superalloy substrate - bond coat system [13,31,41–43]. The reported optimum contents for bulk NiAl alloys or PtAl coatings is around 0.05 to 0.08 at.% for Zr or Y [36]. For doped coatings on a single crystal superalloy, the optimum RE content for TBC lifetime has been reported to be around 0.5 at.% Zr [19]. Additional aspects for TBC performance include the interplay between RE and elements diffusing from the superalloy into the BC, and changes in microstructure during cyclic loading, especially those affecting the TGO adherence. The positive RE-effect on the performance of Ni-based intermetallics is undeniable.

Bond coats are deposited by a variety of methods that mostly rely on atmospheres with reduced oxygen contents to avoid partial oxidation of their elements. In the particular case of NiAl-based coatings vacuum or low-pressure plasma spraying, chemical vapor deposition, pack cementation, EB-PVD, and alternative thermal spraying methods such as HVOF and cold spray are in use or under investigation for bond coat manufacture [16,19,27,44,45]. There are some data in the literature available on NiAl sputtered bond coats on Ni-based superalloys [20,26,32,34,46–49]. Most of them are focused on stoichiometric NiAl, the RE-effect, microstructure, cyclic oxidation behavior, among others. Sputtering offers the unique possibility to exactly tailor and vary the composition of the bond coat. In addition, those PVD coatings are well adherent, highly pure without noticeable oxygen contents, possess a flat surface without any need for further smoothing prior to EB-PVD top coat deposition, and can be tailored to the needs of individual substrate alloys by adjusting the process parameters to create the desired composition, thickness and microstructure. Although the deposition rate is relatively low, more advanced recent sputter coating machines including 4 to 6 sources, better target cooling and advanced arc control provide the opportunity to reach deposition rates in the order of 10 μm/h which offers a great possibility for commercialization, given a batch time of around 3–4 h and a large capacity of several dozens of parts that can be coated simultaneously. However, reports on lifetime behavior of TBC on sputtered bond coats are sparse.

This work reports on microstructure and chemical changes of $\beta + \gamma'$ NiAlCr-X (X = Hf, Zr) bond coats deposited by magnetron sputtering on IN100 and CMSX-4 substrates. Special emphasis was paid on the behavior of EB-PVD 7YSZ top coats under thermal cycling tests at 1100 °C. For comparative purposes, data from NiCoCrAlY and PtAl coatings deposited on similar superalloy substrates are presented and discussed.

2. Experimental procedure

Different sets of bond coats with a planned composition of Ni-36Al-11Cr doped by approx. 0.8 at.% Hf or Zr were deposited on two types of Ni-base superalloy coupons, 6 mm in diameter (commercial cast polycrystalline IN100 or single crystal CMSX-4). These coupons were machined and grinded before coating deposition. No heat treatment was performed to these substrates. Prior to the coating deposition the substrates were cleaned in an ultrasonic bath in isopropanol and then dried with hot air.

The bond coats were deposited by DC-magnetron sputtering in a PVD coater (IMPAX 1000 HT from SVS Karlstad Germany) with four sputtering sources and argon as plasma process gas. The power on the four targets NiAl, Ni, Cr, and X (either Zr or Hf) was defined in pre-trials to achieve the desired composition of the bond coats. Samples were rotated in a two-fold manner as is common when such large coating machines are used to deposit coatings e.g. for cutting tools. The chamber pressure was set to 5.2×10^{-3} mbar and a deposition rate of 2 μm/h was used for this particular set of process parameters to get the selected bond coat composition, while deposition speed was not the main focus of this work. A detailed description of the coater has been reported elsewhere [50]. After bond coat deposition, the samples were heat treated at 1080 °C for 4 h in vacuum of 8×10^{-6} mbar. A standard 7YSZ top coat was deposited on all samples by EB-PVD in a 150 kW coater (ESPRI). Stoichiometric 7YSZ top coats with a standard columnar morphology were achieved. The substrate temperature was maintained between 980° and 1000 °C and the oxygen flow into the coating chamber was controlled to reach a pressure in the chamber between 6 to 8×10^{-3} mbar.

After EB-PVD 7YSZ top coat deposition the samples were named “as coated” to differentiate them from those after furnace cycling tests. Cross sections were prepared by standard metallographic techniques. The samples were characterized by SEM equipped with EDS and EBSD (Carl Zeiss NTS, Germany with Inca EDS and EBSD, from Oxford Instruments, U.K.). Several NiCoCrAlY reference samples with known chemical composition were used to assure reliable compositional data in the EDS system. For the EBSD experiments the samples were prepared after standard metallographic preparation by additional polishing for 30–45 min with a Buehler vibratory polisher. After polishing, the samples were etched for 10 min with Ar plasma. This preparation process reveals the microstructure and assures a stress free surface suitable for EBSD characterization. Selected “as coated” samples were prepared by Focused Ion Beam (FIB) cutting and analyzed via scanning transmission electron microscopy (STEM) in a Phillips Tecnai F30 transmission electron microscope equipped with EDS (EDAX). Thermal cycling was performed at a temperature of 1100 °C in air with a cycle length of 1 h (50 min heating and 10 min cooling down to nearly room temperature) using the DLR FCT set-up. A sample was declared as failed and thus removed when an area of TBC larger than 10 mm in any direction has spalled off. Three samples from each condition were cycled. Table 1 summarizes all sample conditions of this study.

Table 1
Summary of bond coat/superalloy variants and experimental conditions.

Sample ID	Substrate	Condition
NiAlCr-Hf/IN100	IN100	As coated
	IN100	Cycled
NiAlCr-Hf/CMSX-4	CMSX-4	As coated
	CMSX-4	Cycled
NiAlCr-Zr/IN100	IN100	As coated
	IN100	Cycled
NiAlCr-Zr/CMSX-4	CMSX-4	As coated
	CMSX-4	Cycled

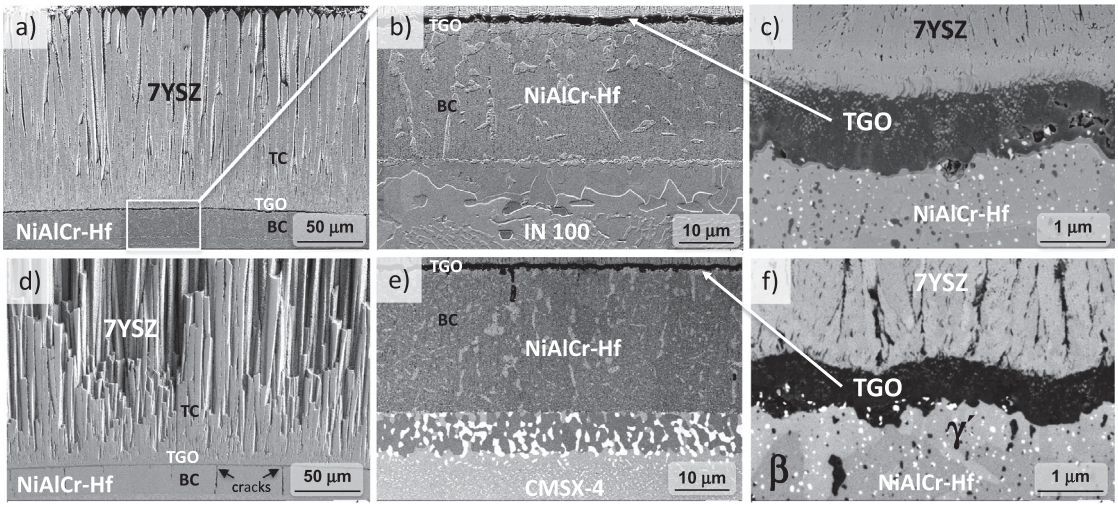

Fig. 1. SEM micrographs recorded in different magnifications of NiAlCr-Hf bond coats sputtered on (a–c) IN 100 and (d–f) CMSX-4 superalloys. These samples are in the "as-coated" condition after deposition of 7YSZ TBC by EB-PVD. Overview of the coating system (a, d), detail of the bond coat including the interdiffusion zone IDZ (b, e), and TGO formation (c, f).

3. Results

3.1. As coated condition

Cross section micrographs of the "as coated" coatings on the two different superalloys are shown at different magnifications (low, medium and high) in Figs. 1 and 2, respectively. The low magnification micrographs (a) and (d) were recorded using the secondary electron detector while images b, c, e, and f were collected using back-scattered electrons to obtain compositional contrast from the IDZ, BC and the TGO. In both sets of samples, the "as coated" bond coats are dense with a homogeneous thickness of around 23 μm. The physical and chemical characteristics of the individual layers were analyzed in detail. For instance, the NiAlCr-Hf/IN100 sample (Fig. 1a–c) shows the following thickness values for BC, TGO, and TC: 21.8 ± 0.5, 1.3 ± 0.1 and 164.5 ± 1.1 μm. In all cases the ceramic top coat was columnar and reached a homogeneous thickness of around 165 μm. A multi-phase IDZ zone of about 8 μm in thickness was identified between the superalloy and the sputtered BC as a result of the vacuum annealing treatment and TC deposition process. The interdiffusion zones from the different sets of samples show some particularities. The IDZ on CMSX-4 contains equiaxed precipitates that can be easily identified by different contrasts through the high atomic number in the backscattering SEM image (see Figs. 1e and 2e), while those precipitates are not present on IN100.

A summary of the thickness and composition data of the "as coated" samples is shown in Table 2. The chemical content of the coatings was measured in cross section (area sections) by EDS in several locations and averaged. The compositions (in at.%) of a standard NiCoCrAlY bond coat deposited by EB-PVD and the used superalloys are included for comparative purposes [9,14,40]. There is a remarkable change in composition of the bond coats after vacuum annealing and TC deposition compared to the as-sputtered conditions (composition was close to Ni-36Al-11Cr-X after sputtering). All elements other than the ternary Ni-Al-Cr-X system from Table 2 result from outward diffusion of elements from the superalloy to the BC. Minor elements present in the superalloys, such as C and B (0.8 and 0.07 at.% in IN100, respectively) are not listed.

The target composition of NiAlCr coatings, aimed to be close to the β-γ′ phase boundary, was successfully achieved. The coatings deposited on IN100 developed a microstructure composed of large and in some cases elongated γ′-grains that are heterogeneously distributed along the BC and continuously formed all along the BC/TGO interface as a result

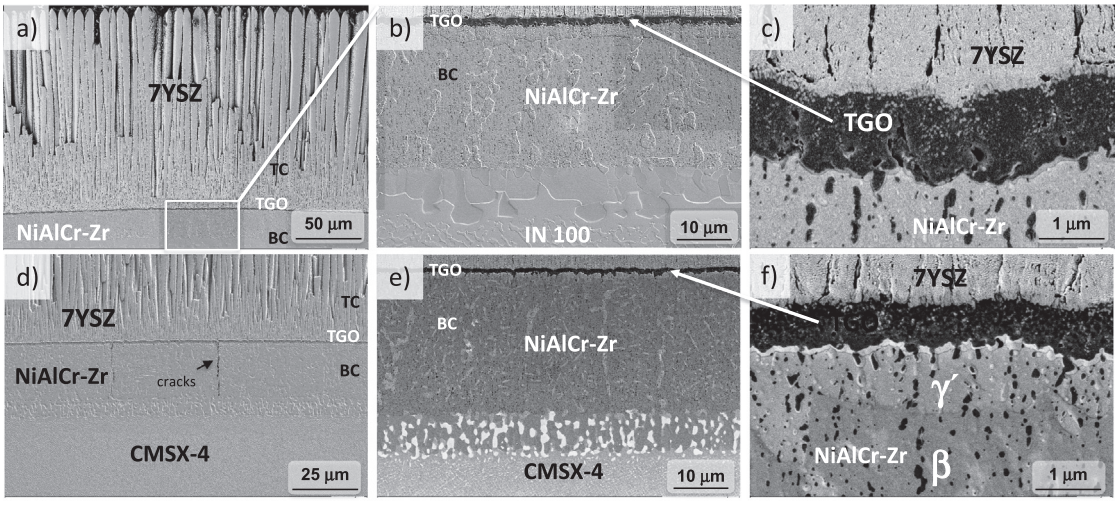

Fig. 2. SEM micrographs recorded in different magnifications of NiAlCr-Zr bond coats sputtered on (a–c) IN100 and (d–f) CMSX-4 superalloys. These samples are in the "as-coated" condition after deposition of the 7YSZ TBC by EB-PVD. Overview of the coating system (a, d), detail of the bond coati including the interdiffusion zone IDZ (b, e), and TGO formation (c, f).

Table 2
Thickness and bond coat composition of the "as coated" samples. Compositions of a NiCoCrAlY coating used as a reference sample as well as IN100 and CMSX-4 superalloys are included.

Sample ID	Thickness (μm)			Composition (at.%)												
	BC	TGO	IDZ	Ni	Al	Cr	Hf	Zr	Co	Ti	Mo	W	Re	Ta	Y	V
NiAlCr-Hf/IN100	21.8 ± 0.1	1.3 ± 0.1	8.1 ± 0.7	56.4	30.5	4.3	0.9	–	5.9	1.8	0.2	–	–	–	–	–
NiAlCr-Zr/IN100	22.7 ± 0.2	1.4 ± 0.1	8.3 ± 0.3	56.0	30.7	4.7	–	0.6	6.1	1.8	0.2	–	–	–	–	–
NiAlCr-Hf/CMSX-4	23.6 ± 0.2	0.9 ± 0.1	7.7 ± 1	57.1	31.2	5.7	0.8	–	3.6	0.4	0.1	0.1	0.1	0.7	–	–
NiAlCr-Zr/CMSX-4	23.2 ± 0.2	0.8 ± 0.1	7.2 ± 1	57.0	32.1	5.4	–	0.7	3.7	0.4	0.1	0.2	0.0	0.6	–	–
NiCoCrAlY	–	–	–	39.1	25.2	17.5	–	–	18.2	–	–	–	–	–	0.1	–
IN100	–	–	–	58.7	10.1	9.4	–	0.03	12.9	5.7	1.3	–	–	–	–	1.07
CMSX-4	–	–	–	63.8	12.6	7.6	0.03	–	9.3	1.3	0.4	2.0	1.0	2.2	–	–

of the outward Al-diffusion process, leading to a distinct Al-depletion zone. On the other hand, the BC deposited on CMSX-4 develops a finer microstructure composed of needle-like γ′-grains, where the Al-depletion zone is smaller. The thickness of the Al-depletion zone is < 1 μm for the CMSX-4 samples and 2–3 μm for the IN100 samples. In addition, a high number of small precipitates that are partly rich in oxygen and either contain Hf or Zr (bright) or Al (dark) are clearly visible in Figs. 1 and 2. Those precipitates will be discussed in detail based on TEM characterization in Section 4.1.

3.2. Furnace cyclic tests

The results of cycles to failure of the TBC systems in FCT at 1100 °C are shown in Fig. 3a. As mentioned before, the number of cycles to failure is reported as an average from three samples in each case. NiAlCr-Zr persevered in average longer on the IN100 than on the CMSX-4 (793 ± 0 and 281 ± 36 cycles, respectively), whereas Hf-addition shows an opposite effect (320 ± 55 and 559 ± 322 cycles for IN100 and CMSX-4, respectively). Thus, it seems that an effect of Zr or Hf doping on the TBC lifetime is also coupled with the effect of substrate composition. Such an effect has been observed previously, e.g. for PtAl the CMSX-4 substrate leads to better TBC performance compared to IN100, whereas for EB-NiCoCrAlY this behavior is inverted [11]. In the same plot, data for EB-NiCoCrAlY and PtAl bond coats deposited either on similar IN 100 or CMSX-4 superalloys and using the same EB-PVD 7YSZ top coat are also shown [9]. The NiAlCr-Hf coating outperforms on CMSX-4 both EB-PVD NiCoCrAlY and PtAl, while on IN100 only NiAlCr-Zr had a lifetime comparable to the reference NiCoCrAlY data.

3.3. Coating characteristics after furnace cyclic tests

Typical SEM micrographs of the samples after FCT are presented in Figs. 4 and 5, respectively. Micrographs shown in a, b and c correspond to the coating systems deposited on IN100 and those from d, e and f to the BC on CMSX-4. Interestingly, the Zr and Hf dopants seem to show different types of failure mechanisms.

TBCs of most samples spalled off mainly at the interface between BC and TGO, whereas in the NiAlCr-Hf/IN100 specimens the TGO remained partially attached to the BC, i.e. partial failure along the interface TBCs/TGO or within the middle of the TGO. Figs. 4b, e and 5b, e show the sections of the IDZ/BC and the interfaces with the corresponding TGO. Compared to the as-coated specimens, the thickness of the BC did not change considerably and remained close to 23 μm in both cases. However, the IDZ increased by 69% in the samples with IN100 superalloy and only by 14% for the samples with CMSX-4 superalloy. After FCT the thickness of the TGO increased to about 6 to 7 μm in all specimens.

As can be seen from Figs. 4a, d and 5a, d, the bond coat deposited on CMSX-4 exhibited radial cracks that were already present in the "as coated" condition, which are subsequently strongly oxidized during FCT. Especially in the NiAlCr-Hf/CMSX-4 BC the previously formed cracks lead to strong internal oxidation in their vicinity (see Fig. 5f). More cracks and oxidized regions in vertical arrangements are visible on CMSX-4 in both the as-coated condition and after FCT compared to IN100 where only a small number of cracks developed only after cycling.

Internal oxidation leading to bright and dark oxide particles is observed in the BC irrespective of the RE-type, see Figs. 4f and 5f. Precipitates are distributed in specific regions of the BC. The bright precipitates mainly contain Hf or Zr and were mostly found in the γ′ phase, while the darker particles are alumina. Large Hf-rich precipitates are found near the boundary of the oxidized cracks as can be seen in Fig. 5f. Most precipitates are present along grain boundaries and within some grains. The amount of alumina particles in the "as coated" condition and after FCT is higher in NiAlCr-Zr on both alloys.

A higher magnification image of the interface BC/TGO in the NiAlCr-Zr/IN100 TBC system is shown in Fig. 4c. The excellent TBC

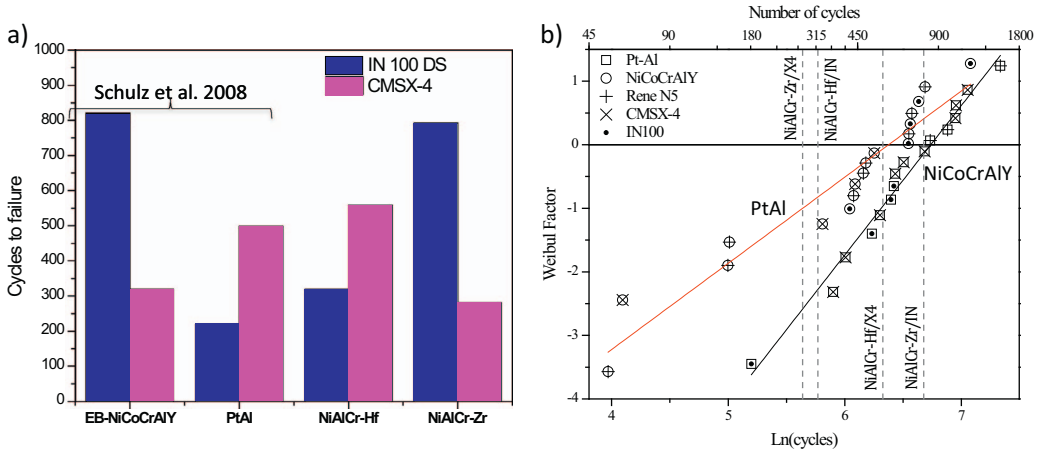

Fig. 3. Cycles to failure of the TBC systems in furnace cyclic testing at 1100 °C. Results of EB-NiCoCrAlY and PtAl bond coats reported elsewhere are shown in (b) as Weibull plots for comparative purposes. (Adapted from Smialek [11]).

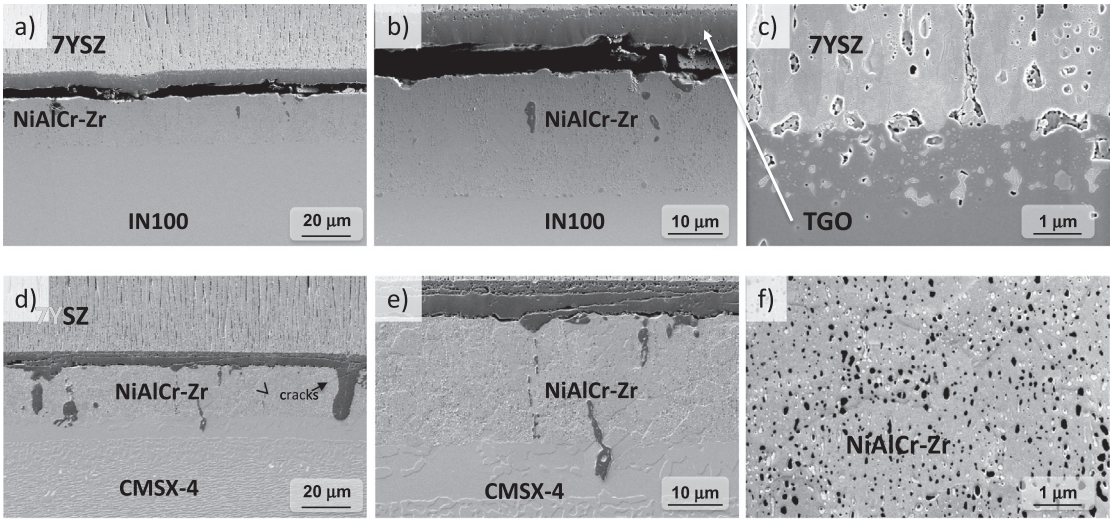

Fig. 4. SEM micrographs recorded in different magnifications of 7YSZ/NiAlCr-Zr TBC samples after FCT at 1100 °C reaching 793 and 284 cycles for these coatings deposited on IN100 and CMSX-4, respectively.

lifetime seems to be due to a good adherence between top coat and TGO, which is associated with a zone formed by a mixture of the EB-PVD 7YSZ and the Al_2O_3 scale. Observations of this zone along the complete sample showed that no failure occurs in the TGO-TC interface. This region, which has been identified and reported by different authors [3,14,51,52] is called a mixed zone, which is a continuous matrix of alumina containing spherodized particles of zirconia. It is already present in the "as coated" condition, (see Fig. 1c and f), but some grains have coarsened during FCT. On the other hand, the BC/TGO interface in the NiAlCr-Hf/IN100 TBC system is shown in Fig. 5c. The formed scale is composed mainly of α-Al_2O_3, and in some areas small layers of nickel aluminates are present, possibly of the type $NiAl_2O_4$ spinel. This is expectable in such a thin bond coat, since the formation of the spinel involves diffusion of Ni through the scale and it is formed under specific partial pressure conditions. Some horizontal cracks growing through the TGO are linked to the presence of the spinel oxides which seems to promote failure within the TGO in the NiAlCr Hf-IN100 samples. It remains unclear why spinels are only found in the TGO for this particular system which is the topic of ongoing research.

4. Discussion

4.1. Bond coat - superalloy interactions in the "as-coated" conditions

4.1.1. Microstructure

As shown in Figs. 1 and 2, the β + γ′ microstructure in our current NiAlCr coatings shows a fairly well fine distribution of γ′ in β after TBC deposition. Since the γ′ is more ductile than β and when it is finely distributed in the β-matrix an enhancement in high temperature strength and higher toughness at room temperature is expected [53]. The distribution of γ′- in the β-matrix depends on several factors in the previous processing steps, such as target composition and sputtering parameters, type of substrate due to specific diffusing elements, annealing temperatures, etc. Especially the substrate temperature during sputtering plays an important role [34]. However, γ′ appears just after TBC deposition mainly due to outward Al-diffusion but also influenced with specific elements diffusing from the substrate.

Other features to notice in the microstructure depending on the substrate type that point out to different bond coat - superalloy interactions already in the "as-coated" condition include the formation of the TGO scale and interdiffusion processes that can lead to phase transformations in the bond coat. A well adherent TGO of homogenous

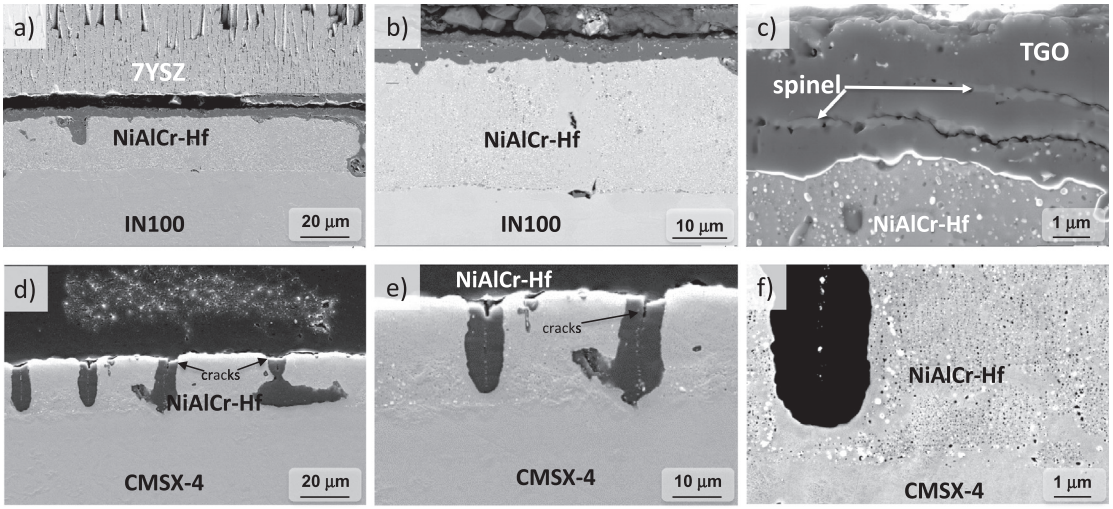

Fig. 5. SEM micrographs recorded in different magnifications of 7YSZ/NiAlCr-Hf TBC samples after FCT at 1100 °C. (a–c) IN100 substrate reaching 384 cycles, and (d–e) CMSX-4 substrate after 924 cycles for these particular coatings.

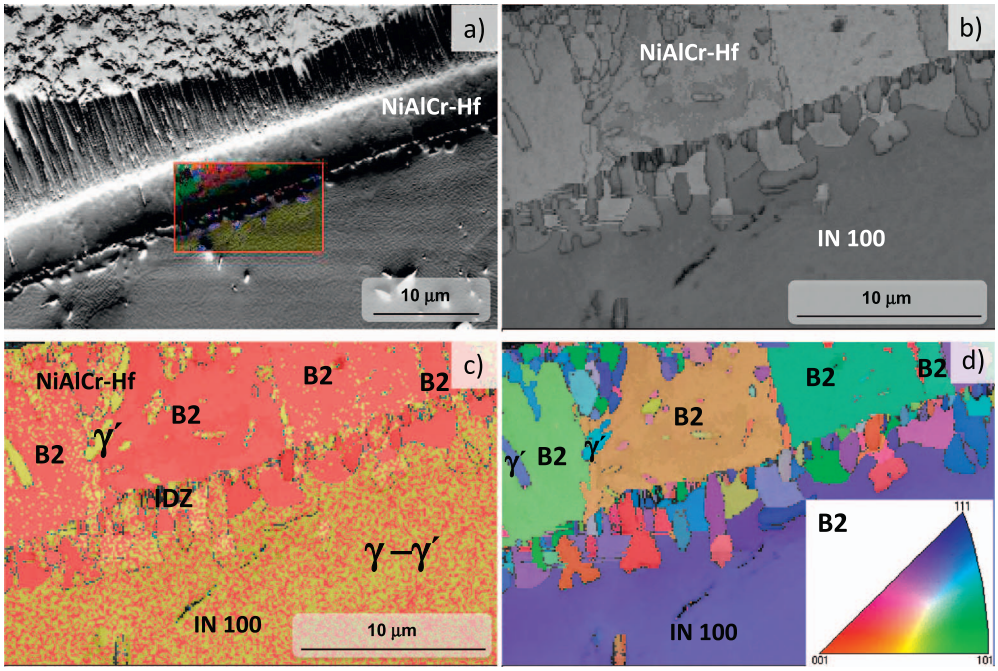

Fig. 6. EBSD analysis for the identification of the phases in the NiAlCr-Hf sputtered bond coat on IN100 after deposition of 7YSZ EB-PVD top coat.

thickness along the cross section is observed for all prepared coatings. The average thickness of the TGO shows slight differences when comparing the samples prepared on IN100 (1.3–1.4 µm) with those on CMSX-4 (0.8–0.9 um), which seems to correlate to the thickness differences in the IDZ, i.e. lower IDZ and TGO thickness for CMSX-4. A reduction in thickness of the IDZ in magnetron sputtered β-NiAl on CMSX-4 due to Hf-additions compared with undoped coatings has been reported [26,34,46]. In our coatings, the IDZ thickness is nearly the same for Hf and Zr additions, but varies slightly between the substrates. Since annealing and EB-PVD deposition was done for all coatings at the same time, the reason for these differences is associated to differences in composition due to the elements diffusing from the superalloys to the bond coat. Co, Ti and Mo are common elements from the IN100 and CMSX-4 diffusing to the BC proportional to their contents in the superalloy. In IN100 the Ti content is high (4.7 at.%) and Ti diffuses into the bond coats already during vacuum annealing and during TC deposition to a much higher extent (1.8 at.%) than on CMSX-4 (0.4 at.%, see Table 2). The slightly slower initial oxidation kinetics in the BC deposited on CMSX-4 can be also related to the effect of additional elements diffusing from CMSX-4 (Ta, W, Re) that are not present in IN100. The combined effect of Ti-Hf has been reported to be detrimental to the oxidation behavior compared with single Hf-additions in NiAl bond coats [36]. Moreover, Ti can be harmful specifically to the oxidation kinetics of the $L1_2$-phase at 1100 °C [54]. In our particular case, the Ti-content from the IN100 substrate increases the TGO thickness irrespective of the RE-doping. There were only minor differences in TGO thicknesses between the Hf and Zr doped version that are within the measurement uncertainty.

The TGO consists of a typical mixture of zirconia particles embedded in alumina, especially in the upper part. In some areas this mixture is not continuous in plane indicative of the following scenario: During vacuum annealing the elements with high mobility and the highest oxygen affinity (Hf and Zr in the present case) start to oxidize on the surface of the bond coat. In the areas surrounding those oxide particles transient alumina can form, mainly during the top coat deposition. It is well known that this transient alumina can dissolve considerable amounts of zirconia, but during subsequent transformation to stable α-Al_2O_3 the excess ZrO_2 is precipitated, leading to the mentioned mixed zones. Underneath or in the RE-oxides particles no dissolution of zirconia occurs, and hence no subsequent re-precipitation of zirconia is observed, and the TGO consists of pure alumina, visible in Fig. 1c and d as the continuous dark regions. A Ni enrichment underneath the TGO that leads to the formation of the γ′-phase was observed as a result of the Al consumption.

Vertical cracks were occasionally observed in the bond coats on CMSX-4. Those defects show a thin alumina layer along the crack edges, occasionally through the whole BC thickness. The reasons to have specifically these defects only on CMSX-4 remain unclear at this stage but might be associated to the intrinsic brittleness of NiAl, the columnar growth mechanism typical from sputtering [55], combined with tensile residual stresses present in the coatings due to differences in the coefficient of thermal expansion between the BC and the superalloys. However, considering the CTE values at 1000 °C of NiAl (α_c = 15.1 ppm/°C) [56], Ni_3Al (α_c = 19 ppm/°C) [57], CMSX-4 (α_s = 15.7 ppm/°C) [56] and IN100 (α_s = 16.3 ppm/°C) [56] one can see that the difference α_s - α_c, which is proportional to the residual tensile stress, is larger in IN100 and hence CTE differences alone cannot explain the more frequent crack formation in the coatings on CMSX-4 [58]. Another reason might be the polycrystalline versus single crystal condition of the used superalloys and the anisotropy of the CTE in the single crystal. Current ongoing research focuses on avoiding the formation of these defects in the NiAlCr-X coatings on CMSX-4. These defects seem to have an influence on the failure mechanisms of the TBC but only limited implications for TBC lifetime (see Fig. 3a), since for Hf doping the lifetime on CMSX-4 is longer than on IN100.

The presence of the β and γ′ phases in the bond coats is confirmed by the combination of EDS and EBSD results from cross sections. Fig. 6 shows a typical set of EBSD results in the NiAlCr-Hf sputtered bond coat on IN100 after deposition of the 7YSZ EB-PVD top coat. The analyzed zone is shown in Fig. 6a, while Fig. 6b shows the topography image in a grey scale of the scanned area and corresponds to the zone at the interface between the IN100 alloy substrate and the NiAlCr-Hf bond coat. The topography image from Fig. 6b is partially comparable to those presented in Figs. 1b and 2b with the difference in orientation, i.e. a 70° rotation to carry out the EBSD analysis. Fig. 6c displays the B2 and $L1_2$ phase distribution in the BC-IDZ-Substrate zone. The B2 crystals found in the BC are depicted in red and γ′ in yellow. As expected, the γ + γ′ phases in the substrate alloy are all displayed in a single color, since EBSD cannot clearly distinguish between these two phases. The crystal orientation is shown in Fig. 6d. A random orientation of B2 grains is

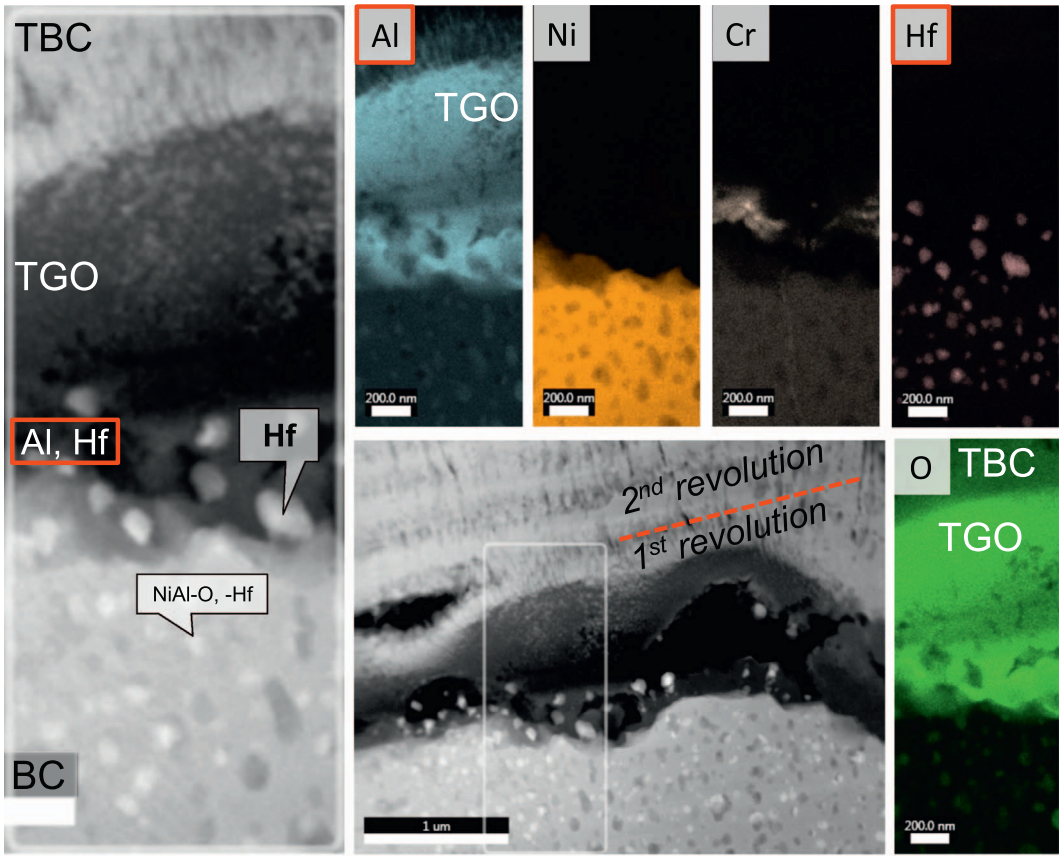

Fig. 7. STEM micrograph and EDS maps from the boxed area (left) in the bright field STEM image (middle bottom) of the FIB cut from the cross-section of a BC/TGO interface of the "as coated" NiAlCr-Hf/IN100 sample.

observed, where the big ones are closely oriented to the [101] direction. In general, both types of BC consist of a mixture of β + γ′ phases. The grains in the IDZ are also randomly oriented in all three crystallographic directions and in the BC the γ′ are at the borders of the B2 grains and closely oriented to the [111] direction (Fig. 6d).

4.1.2. Detailed analyses by TEM

Further analysis of the chemical composition obtained by STEM at the interface between BC and TGO in the "as coated" NiAlCr-Hf/IN100 sample is shown in Figs. 7 and 8. The STEM work presented in Fig. 7 confirms that the BC is composed of a mixture of γ′ and B2 phases and fine particles of different nature that are precipitated all along the BC. The boxed area shown in the bottom bright field STEM micrograph in the middle was analyzed by EDS mapping. The TGO is mainly composed of aluminum oxide containing zirconia particles (not shown here), with some traces of chromium oxide and enclosed Hf-oxide

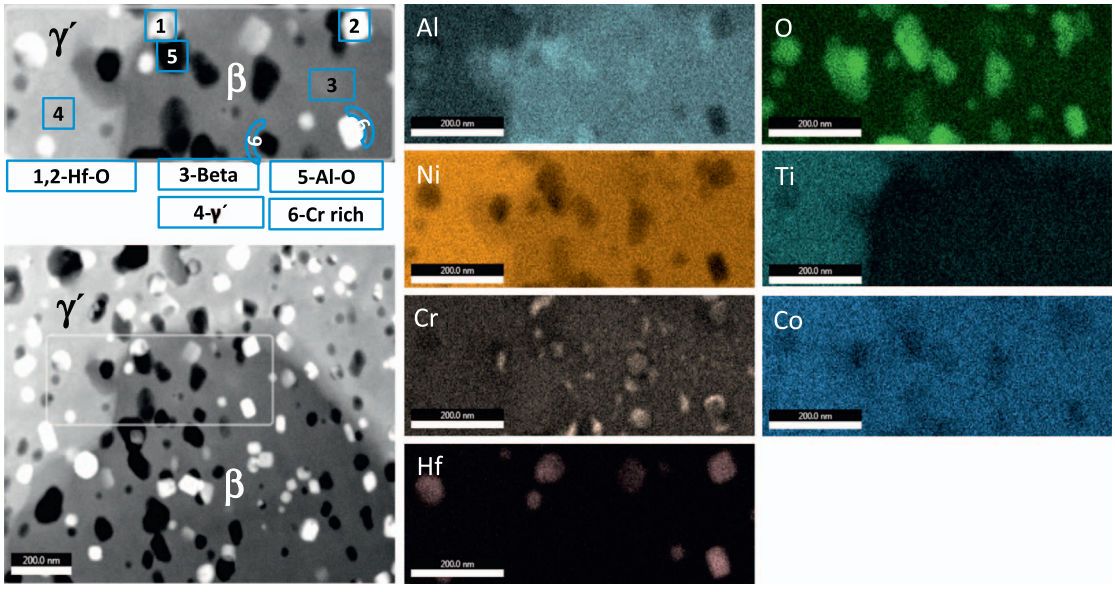

Fig. 8. STEM micrograph (bottom left) and EDS maps from the boxed area (top left) from a region of the NiAlCr-Hf BC in the "as coated" condition on IN100.

particles close to the BC interface. In the BC, round shaped particles with different contrasts of approximately 100 nm in diameter were identified homogeneously distributed in the BC. According to the combination of elements (Al, Ni, Cr, Hf and O) and their contrast, these particles are either rich in hafnium and oxygen (bright particles) or contain mostly aluminum and oxygen (darker particles). These internal Hf-rich oxide particles have been reported to be beneficial to the overall furnace cyclic life of the coatings since it is supposed to improve scale adhesion [29]. On the other hand, the RE-effect is more efficient once the dopant is metallic. However, as mentioned before, the biggest effect seems to come from the type of substrate chemistry, in which the combination IN100 with NiAlCr-Zr leads to the best performance.

A set of bright field STEM/EDS micrographs from the middle of the NiAlCr-Hf BC on IN100 recorded at higher magnifications are shown in Fig. 8. In this case, the EDS boxed area shown in the bottom-left bright field STEM micrograph was chosen to confirm the nature of the BC grains observed as bright and dark contrast as well from the particles with different colors. Additional to the EDS mapping, point analysis was done in the particles (identified as 1, 2, 5 and 6) as well as in the matrix of the BC grains (identified as 3 and 4). Measurements (not shown here) confirmed the γ′ and B2 phases for the bright and dark BC grains, respectively. Additional observations are the preference of Co, and specially Ti to diffuse to the γ′ grains. Regarding the particles, the composition of the bright colored ones showed almost pure HfO_2 as observed from points analysis 1 and 2, while the dark colored ones correspond to Al_2O_3 particles. At this stage it remains unclear why the bond coat shows already in the "as coated" stage this heavy internal oxidation, leading to numerous Hf- and Al-oxide particles. It is assumed that the sputtered bond coat which exhibits a slight columnar microstructure after deposition was not fully dense. The subsequent vacuum annealing initiated further crystallization and grain grow of the β-and γ′-phases, and some oxygen has penetrated into the coating that led to the oxide particles formation. Since magnetron sputtering is done in a very low oxygen partial pressure regime, a possible oxygen solution within the BC during PVD is ruled out. Fig. 8 indicates a Cr-rich layer that surrounds the alumina grains (point 6). In essence, the TEM work confirmed the findings given above for phase composition and element partitioning, TGO growth, and nature of the particles.

4.1.3. Quantification of phases

A phase quantification was done by image analysis from at least three SEM micrographs. The NiAlCr-Hf or NiAlCr-Zr coatings deposited either on IN100 or CMSX-4 showed γ′ contents of 15.3% and 17%, or 14.6% and 16.2%, respectively (see Table 3). This measured content is compared to calculate data based on normalizing the measured chemical composition to a Ni-Al-Cr phase diagram by taking into account the specific sublattice occupancy of the elements. Representing the chemical composition of higher order multicomponent systems such as superalloys on a ternary phase diagram e.g. Ni-Al-Cr using the sublattices approach has been discussed in the literature [59,60]. A sublattices model can be applied to a multiple phase system and considers interaction of the elements between the sublattices and on the sublattice itself [59]. In the present case, the Ni-Al-Cr coatings develop a multiphase structure after diffusion processes from the superalloy due to processing steps or previous heat treatments. As mentioned before, even in the "as coated" conditions the coatings showed the presence of several other elements such as Co, Ti, Mo diffused from IN100 or Re, W and Ta from CMSX-4.

Table 3
Summary of phase content as determined by image analysis from SEM micrographs and applying the lever rule to a Ni-Al-Cr phase diagram based on the sublattices model.

Sample ID	Normalized data (at.%)			Image analysis		Phase diagram lever rule	
	Ni	Al	Cr	β	γ′	β	γ′
NiAlCr-Hf/IN100	63.1	32.6	4.3	84.8	15.3	94.5	5.5
NiAlCr-Zr/IN100	62.4	32.7	4.9	85.4	14.6	90.4	9.6
NiAlCr-Hf/CMSX-4	62.4	31.8	5.8	83.0	17.0	90.7	9.3
NiAlCr-Zr/CMSX-4	62.0	32.6	5.4	83.8	16.2	97.6	2,4

The average chemical composition of the bond coats was obtained from EDS measurements of areas covering most of thickness in cross sections, excluding the Al depletion zones close to the TGO and IDZ. The experimental data was allocated to the Ni-Al-Cr ternary system from the identified elements (Ni, Al, Cr, Co, Ti, Mo, Re, Hf, Zr, W, Ta, V) according to site preferences criteria of transition elements recently reported by Jiang [61]. This method is based on the Bragg-Williams approximation, were the bond strength between pairs of atoms of every sublattice is calculated with ternary additions of X = Cr, Co, Ti, Mo, Re, Hf, Zr, Ta, W and others. For the β-phase, Co and Re have a consistent site preference for the Ni site and Ti, Hf, Zr and Ta have a preference for the Al site. However, Cr, W and Mo have a composition and temperature dependency of their site preferences.

In the simplest case the Jiang model is applied only to the B2-phase. This leads to the following normalization model at 1100 °C: (Al + Ti + Zr + 0.58Mo + Hf + W + Ta + V) (Ni + Co + 0.42Mo + Re). In other words, Ti, Zr, Hf, W, Ta, V and 58% of the Mo content occupy Al sites, whereas, Co, Re and 42% of the Mo content goes to the Ni sites. The measured contents of those elements were added to the respective amounts of Ni and Al following the procedure described above, as detailed in Table 3. This allowed plotting the measured average composition data of a multi-element system in the ternary Ni-Al-Cr phase diagram, see open symbols in Fig. 9. These points are allocated either close to the boundary (NiAlCr-Zr/CMSX-4) or already within the β-γ′ region in the β-rich zone. For comparative purposes, the measured composition of the β or γ′-phases in NiAlCr-Hf/IN100 are also shown derived from EDS point analyses. These points are not exactly allocated on the β + γ′ field boundaries of the phase diagram [62], which can be due to different reasons: a) correctness of normalization method, b) EDS calibration uncertainty, c) phase diagram incorrectness or d) phases are not in equilibrium.

Taking into account the average measured composition of the areas (open symbols in Fig. 9) and applying the lever rule, the presence of γ′ is predicted in all coatings. However, the predicted content shows in all cases a deviation from the data obtained by image analyses from micrographs. A summary of results is shown in Table 3. It is worth to mention that another source of deviation between the experimental normalized data and the limits and phase contents is because the Jiang model only considers the total potential electrostatic energy and configurational entropy, but neglects the vibrational entropy, which may play an important role in determining the site preferences. Furthermore, contributions such as thermal defects, stresses, voids and interaction parameters between elements are not considered in the theoretical model. Even the simple model of a single beta phase and normalizing the elements in a sublattice concept helps to predict the phase content. It does not fully match with the phase contents obtained by image analysis from Figs. 1 and 2 for the reasons given above, but shows general trends well. Finally, the normalized composition of NiCoCrAlY coatings is also shown in Fig. 9 for comparative purposes.

Additional chemical point or line analyses (not shown here) were performed to identify composition gradients in the sputtered bond coats. In general, the Cr content does not change along the BC thickness, but shows lower values in the γ′ phase. The reason is that Cr has a lower activity and solubility in γ′ than in the β-phases. On the contrary, the Ti content was found to be higher in the γ′ phase than in β which can be expected since titanium is an element with preference for γ′. The

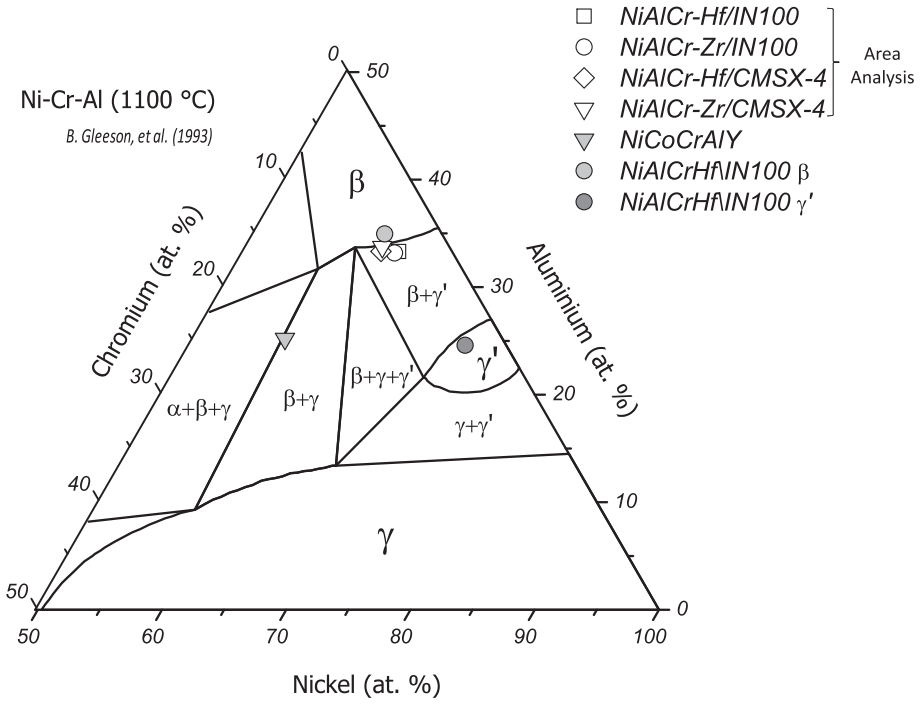

Fig. 9. Ni-Rich isothermal section of the Ni-Al-Cr phase diagram after [62] showing chemical composition data measured by EDS (AREA) of the BC cross sections of the "as-coated" samples. Results of the NiAlCr-Hf/IN100 coating measured by point measurements as well as from a standard NiCoCrAlY coating are shown for comparative purposes.

NiAlCr-Hf or -Zr coatings deposited on IN100 show always higher contents of Ti and Mo, whereas NiAlCr-Hf or -Zr coatings deposited on CMSX-4 showed higher values of Co and the presence of W, Re and Ta. The content of elements diffusing from the substrate into the bond coats and the differences between the two substrate alloys can be explained with the respective contents in the substrates with the exception of Co that has a slightly lower content in CMSX-4 than in IN100, but a higher content in the NiAlCr-X/CMSX-4 version.

4.2. Lifetime and microstructural features after failure

Typical effects associated with high temperature exposure of those coatings such as changes in composition and phase contents, TGO thickening, and interdiffusion were observed. This increase in interdiffusion zone thickness is caused by ongoing interdiffusion of elements between superalloy and bond coat during the furnace cyclic tests. The differences between the two superalloys can be explained by different thermodynamic driving forces (i.e. different activities) for interdiffusion due to differences in substrate alloy composition, but this was not the main focus of this study. There was no rumpling observed in the current coating, although it is frequently observed on coatings that contain high amounts of the beta-phase such as NiPtAl – 7YSZ systems [63]. The absence of rumpling is a potential advantage of the sputtered coating since the associated TBC failure mechanism can be avoided.

4.3. TGO evolution

Based on cross sections of the coatings after FCT, TGO thicknesses were measured and plotted over the number of cycles. Fig. 10 gives experimental data of the sputtered bond coats and a power law fit for a EB-PVD NiCoCrAlY bond coat deposited on the same superalloys for comparison (data are taken from [40,64]). A fit using the following power law was performed: $TGO_{thickness} = 1.67N_{cycles}^{0.22}$. The NiAlCr-Hf/CMSX-4 sample is not included since the failure characteristics did not allow for determination of the TGO thickness. It is evident that our current data follows completely the tendency marked by the NiCoCrAlY coatings, irrespective of the superalloy type. There is no clear influence of Hf or Zr doping on the oxidation rates, most likely due to the partial oxidation of the RE-addition in the "as coated" condition and perhaps over-doping discussed below, although no data for an un-doped reference NiAlCr coating of the same composition is available.

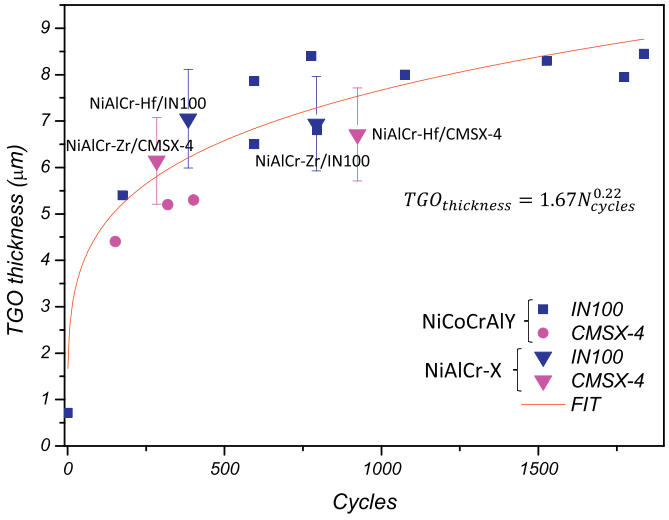

Fig. 10. Experimental data and a power law fit of the TGO thickness vs number of cycles to failure of the NiAlCr-X 7YSZ TBC systems in comparison to NiCoCrAlY data taken from [40].

4.4. Lifetime

The current results of lifetime can be compared with a broader literature data source. For instance, Fig. 3b shows the selected data taken from [11] from PtAl and NiCoCrAlY bond coats tested at 1100 °C and deposited on three different superalloys: CMSX-4, ReneN5 and IN100. The data are represented in separate Weibull plots for either PtAl or NiCoCrAlY differentiating in each case the type of substrate. From this graph it is clear that the PtAl coatings show a closer data distribution (higher Weibull slope) than NiCoCrAlY coatings meaning a higher reproducibility in the cycles to failure and a tendency to show higher number of cycles when deposited on ReneN5 and the lower performance on IN100. NiCoCrAlY coatings deposited on IN100 show a

tendency to behave better than on CMSX-4. In a similar way our bond coats clearly show a mixed influence of the substrate and the doping type.

Our results on the cyclic TBC lifetime are identified in the plot from Fig. 3b as vertical discontinuous lines in order to directly compare their lifetime with literature data. The NiAlCr-Zr/IN100 coatings showed the longest lifetime (793 cycles, respectively), which is nearly equal to that of a much thicker NiCoCrAlY standard PWA1370-type bond coat and according to the plot shown in Fig. 3b close to the general average lifetime of PtAl coatings. Although the lifetime on Hf-doped NiCoCrAlY coatings deposited by EB-PVD is much higher (~3000 cycles for approx. 0.15 at.% and ~4700 cycles for approx. 0.25 at.% Hf) [9] than that on the current sputtered BC, these layers cannot be directly compared since the thickness of the current BC is much smaller and its dopant level is much higher. Considering that even in the "as-coated" condition strong diffusion processes already took place, the good performance of the present coatings indicates that our sputtered bond coats provide a promising alternative for TBC application, despite their low thickness. The current results indicate that magnetron sputtering is a promising technique for creation of chemically well-controlled, well adherent bond coats that provide adequate TBC lifetimes. The bond coats can be tailored to the needs of individual substrate alloys by adjusting the process parameters to create the desired composition, thickness and microstructure. Further work to optimize the sputtered bond coats in terms of composition and microstructure is under way to prolong the TBC lifetime and to fully benefit from the RE-effect.

The long lifetime of TBCs on β-NiAlCr + Zr might be attributed to several factors; (i) lower Al diffusion, (ii) segregation of Zr to the scale-metal interface and the scale grain boundaries, which is an effect previously demonstrated elsewhere e.g. by SIMS analysis through grain boundaries in NiAl [33], or (iii) reduced cation diffusion as shown by Kitaoka [65]. In his contribution Y and Hf doping for alumina scale growth and diffusion in terms of electron density of states is discussed [65]. In the ideal case for high purity bulk alumina, Kitaoka has shown that cation diffusion can be reduced by Hf doping while anion diffusion was reduced by Y doping. Our results may indicate that TBC spallation and dopant effects are more complex than simply grain boundary diffusion and alumina scale thickness as predicted from basic diffusion studies. Other possible reason why in the present study no clear influence of Hf or Zr-doping was obtained is that the RE content might already be too high, i.e. the BC is over-doped which typically leads to a drastic reduction in the lifetime [11]. On the other hand, most RE-containing particles in the BC are already oxidized in the "as coated" condition due to internal oxidation during vacuum annealing and TC deposition, as shown by the detailed TEM analyses described above, and it is known that the RE-effect is more effective when the dopant is present in metallic form rather than as oxide [36].

5. Conclusions

The effects of approx. 0.8 at.% Zr or Hf-additions to NiAlCr coatings deposited by magnetron sputtering onto CMSX-4 and IN100 substrates on the performance of 7YSZ EB-PVD TBCs is rather complex since it relies on a combination of several factors that include physical and chemical properties of the superalloy, the bond coat, and interactions of both. The following conclusions were obtained:

1. In the "as coated" condition (which is after vacuum annealing of the bond coat and top coat deposition) the bond coats consist of a $\beta - \gamma'$ phase mixture. Elements from the substrate have already diffused into the relatively thin (23 μm) bond coat in amounts depending on the superalloy type. The measured composition was normalized to a ternary Ni-Al-Cr system following the theoretical guidelines of site preferences of alloying elements leading to a $\beta - \gamma'$ phase mixture that matches the experimental observation quite well.
2. The bond coat contains internal oxide particles that are either Hf or Al-rich. Irrespective of the Zr or Hf-additions, the CMSX-4 substrate leads to the formation of crack-wise defects in the bond coat that only slightly affected the lifetime of these coatings.
3. Both substrate and dopant type have a clear influence on TBC lifetime. Zr-additions to the NiAlCr bond coat lead to a clearly better TBC performance on the IN100 than on CMSX-4 (793 and 281, respectively) whereas Hf-additions show an opposite effect (320 and 559 cycles). The TBC lifetimes of the best version NiAlCrZr/IN100 were adequate to much thicker standard NiCoCrAlY bond coats, while the NiAlCrHf/CMSX-4 version was even better than PtAl or NiCoCrAlY based systems on the same alloy.

Acknowledgements

This project has been supported by CONACyT-BMBF through the grants Nr. 174178 and 224253 and partially done at CENAPROT and LIDTRA national laboratories. J.M.S. thanks the Alexander von Humboldt Foundation for financial support for research activities at the German Aerospace Center (DLR). The authors thank J. Brien, D. Peters and A. Handwerk for coating manufacture and testing, P. Watermeyer for helping with EBSD and for performing the TEM work and A. Mora García for general support.

References

[1] D.R. Clarke, M. Oechsner, N.P. Padture, Thermal-barrier coatings for more efficient gas-turbine engines, MRS Bull. 37 (2012) 891–898, http://dx.doi.org/10.1557/mrs.2012.232.
[2] R. Darolia, Thermal barrier coatings technology: critical review, progress update, remaining challenges and prospects, Int. Mater. Rev. 58 (2013) 315–348, http://dx.doi.org/10.1179/1743280413Y.0000000019.
[3] M.J. Stiger, N.M. Yanar, M.G. Topping, F.S. Pettit, G.H. Meier, Thermal barrier coatings for the 21st century, Zeitschrift Fur Met. 90 (1999) 1069–1078 http://cat.inist.fr/?aModele=afficheN&cpsidt=1214642.
[4] M. Peters, C. Leyens, U. Schulz, W.A. Kaysser, EB-PVD thermal barrier coatings for aeroengines and gas turbines, Adv. Eng. Mater. 3 (2001) 193–204, http://dx.doi.org/10.1002/1527-2648(200104)3:4<193::AID-ADEM193>3.0.CO;2-U.
[5] C.G. Levi, Emerging materials and processes for thermal barrier systems, Curr. Opin. Solid State Mater. Sci. 8 (2004) 77–91, http://dx.doi.org/10.1016/j.cossms.2004.03.009.
[6] V.K. Tolpygo, D.R. Clarke, K.S. Murphy, Oxidation-induced failure of EB-PVD thermal barrier coatings, Surf. Coat. Technol. 146–147 (2001) 124–131, http://dx.doi.org/10.1016/S0257-8972(01)01482-7.
[7] J.M. Alvarado-Orozco, R. Morales-Estrella, M.S. Boldrick, G. Trapaga-Martinez, B. Gleeson, J. Munoz-Saldana, Kinetic study of the competitive growth between theta-Al_2O_3 and alfa-Al_2O_3 during the early stages of oxidation of B2-(Ni,Pt)Al bond coat systems: effects of low oxygen partial pressure and temperature, Metall. Mater. Trans. A Phys. Metall. Mater. Sci. 46 (2014) 726–738, http://dx.doi.org/10.1007/s11661-014-2669-3.
[8] L.A. Cáceres-Díaz, J.M. Alvarado-Orozco, H. Ruiz-Luna, J. Edison García-Herrera, A.G. Mora-García, G. Trápaga-Martínez, R. Arroyave, J. Muñoz-Saldaña, H. Lopez, Study of the isothermal oxidation process and phase transformations in B2-(Ni,Pt)Al/RENE-N5 system, Metals (Basel) 6 (2016) 1–13, http://dx.doi.org/10.3390/met6090208.
[9] U. Schulz, K. Fritscher, A. Ebach-Stahl, Cyclic behavior of EB-PVD thermal barrier coating systems with modified bond coats, Surf. Coat. Technol. 203 (2008) 449–455, http://dx.doi.org/10.1016/j.surfcoat.2008.08.056.
[10] H. Lau, C. Leyens, U. Schulz, C. Friedrich, Influence of bond coat pre-treatment and surface topology on the lifetime of EB-PVD TBCs, Surf. Coat. Technol. 165 (2003) 217–223, http://dx.doi.org/10.1016/S0257-8972(02)00726-0.
[11] J.L. Smialek, Compiled furnace cyclic lives of EB-PVD thermal barrier coatings, Surf. Coat. Technol. 276 (2015) 31–38, http://dx.doi.org/10.1016/j.surfcoat.2015.06.018.
[12] I.G. Wright, B.A. Pint, W.Y. Lee, K.B. Alexander, K. Pruessner, Some effects of metallic substrate composition on degradation of thermal barrier coatings, High Temp. Surf. Eng. (1997) 95–113 (%5C%5CKwi-server%5Cliteratur%5Cedo%5Carticles%5CDSH%5CDSH_0892.pdf).
[13] B. Pint, I. Wright, W. Lee, Y. Zhang, K. Prüßner, K. Alexander, Substrate and bond coat compositions: factors affecting alumina scale adhesion, Mater. Sci. Eng. A 245 (1998) 201–211, http://dx.doi.org/10.1016/S0921-5093(97)00851-4.
[14] U. Schulz, M. Menzebach, C. Leyens, Y.Q. Yang, Influence of substrate material on oxidation behavior and cyclic lifetime of EB-PVD TBC systems, Surf. Coat. Technol. 146–147 (2001) 117–123, http://dx.doi.org/10.1016/S0257-8972(01)01481-5.
[15] R.T. Wu, K. Kawagishi, H. Harada, R.C. Reed, The retention of thermal barrier coating systems on single-crystal superalloys: effec1 R.T. Wu, K. Kawagishi, H. Harada, and R.C. Reed, Acta Mater. 56, 3622 (2008).ts of substrate composition, Acta Mater. 56 (2008) 3622–3629, http://dx.doi.org/10.1016/j.actamat.2008.03.046.

[16] V.K. Tolpygo, K.S. Murphy, D.R. Clarke, Effect of Hf, Y and C in the underlying superalloy on the rumpling of diffusion aluminide coatings, Acta Mater. 56 (2008) 489–499, http://dx.doi.org/10.1016/j.actamat.2007.10.006.
[17] R. Darolia, NiAl alloys for high-temperature structural applications, JOM 43 (1991) 44–49, http://dx.doi.org/10.1007/BF03220163.
[18] A.I. Kovalev, R.A. Barskaya, D.L. Wainstein, Effect of alloying on electronic structure, strength and ductility characteristics of nickel aluminide, Surf. Sci. (2003) 35–40, http://dx.doi.org/10.1016/S0039-6028(03)00208-5.
[19] B. Hazel, J. Rigney, M. Gorman, B. Boutwell, R. Darolia, Development of improved bond coat for enhanced turbine durability, Proc. Int. Symp. Superalloys, 2008, pp. 753–760.
[20] M.A. Bestor, J.P. Alfano, M.L. Weaver, Influences of chromium and hafnium additions on the microstructures of β-nial coatings on superalloy substrates, Intermetallics 19 (2011) 1693–1704, http://dx.doi.org/10.1016/j.intermet.2011.06.020.
[21] S. Wu, X. Wu, R. Wang, Q. Liu, L. Gan, Effects of Ni vacancy, Ni antisite, Cr and Pt on the third-order elastic constants and mechanical properties of NiAl, Intermetallics 55 (2014) 108–117, http://dx.doi.org/10.1016/j.intermet.2014.04.022.
[22] L. Zhou, S. Mukherjee, K. Huang, Y.W. Park, Y. Sohn, Failure characteristics and mechanisms of EB-PVD TBCs with Pt-modified NiAl bond coats, Mater. Sci. Eng. A 637 (2015) 98–106, http://dx.doi.org/10.1016/j.msea.2015.03.120.
[23] C.A. Barrett, Oxid. Met. 30 (1988) 361, http://dx.doi.org/10.1007/BF00659006.
[24] D. Wang, H. Peng, S. Gong, H. Guo, NiAlHf/Ru: promising bond coat materials in thermal barrier coatings for advanced single crystal superalloys, Corros. Sci. 78 (2014) 304–312, http://dx.doi.org/10.1016/j.corsci.2013.10.013.
[25] B.A. Pint, Progress in understanding the reactive element effect since the Whittle and Stringer literature review, in: P.F. Tortorelli, I.G. Wright, P.Y. Hou (Eds.), John Stringer Symp. High Temp. Corros, ASM International, 2003, pp. 9–19.
[26] M.A. Bestor, R.L. Martens, R.a. Holler, M.L. Weaver, Influences of annealing and hafnium concentration on the microstructures of sputter deposited β-NiAl coatings on superalloy substrates, Intermetallics 18 (2010) 2159–2168, http://dx.doi.org/10.1016/j.intermet.2010.07.001.
[27] S. Hamadi, M.P. Bacos, M. Poulain, A. Seyeux, V. Maurice, P. Marcus, Oxidation resistance of a Zr-doped NiAl coating thermochemically deposited on a nickel-based superalloy, Surf. Coat. Technol. 204 (2009) 756–760, http://dx.doi.org/10.1016/j.surfcoat.2009.09.073.
[28] A. Strawbridge, P.Y. Hou, The role of reactive elements in oxide scale adhesion, Mater. High Temp. 12 (1994) 177–181, http://dx.doi.org/10.1080/09603409.1994.11689484.
[29] D.P. Moon, Role of reactive elements in alloy protection, Mater. Sci. Technol. 5 (1989) 754–764, http://dx.doi.org/10.1179/mst.1989.5.8.754.
[30] B.A. Pint, Experimental observations in support of the dynamic-segregation theory to explain the reactive-element effect, Oxid. Met. 45 (1996) 1–37.
[31] D. Li, H. Guo, D. Wang, T. Zhang, S. Gong, H. Xu, Cyclic oxidation of β-NiAl with various reactive element dopants at 1200 °C, Corros. Sci. 66 (2013) 125–135, http://dx.doi.org/10.1016/j.corsci.2012.09.010.
[32] S. Hou, S. Zhu, T. Zhang, F. Wang, A magnetron sputtered microcrystalline β-NiAl coating for SC superalloys. Part I. Characterization and comparison of isothermal oxidation behavior at 1100 °C with a NiCrAlY coating, Appl. Surf. Sci. 324 (2015) 1–12, http://dx.doi.org/10.1016/j.apsusc.2014.10.106.
[33] E. Schumann, J.C. Yang, M. Rühle, M.J. Graham, The effect of Y and Zr on the oxidation of NiAl, MRS Proc. 364 (1995) 1291–1296, http://dx.doi.org/10.1557/PROC-364-1291.
[34] B. Ning, M. Shamsuzzoha, M.L. Weaver, Influence of processing variables on the properties of dc magnetron sputtered NiAl coatings containing Hf additions, J. Vac. Sci. Technol. A Vac. Surf. Film. 23 (2005) 44, http://dx.doi.org/10.1116/1.1828085.
[35] C. Leyens, B.a. Pint, I.G. Wright, Effect of composition on the oxidation and hot corrosion resistance of NiAl doped with precious metals, Surf. Coat. Technol. 133–134 (2000) 15–22, http://dx.doi.org/10.1016/S0257-8972(00)00878-1.
[36] B.A. Pint, K.L. More, I.G. Wright, Effect of quaternary additions on the oxidation behavior of Hf-doped NiAl, Oxid. Met. 59 (2003) 257–283, http://dx.doi.org/10.1023/A:1023087926788.
[37] A. Strawbridge, R.A. Rapp, The role of reactive elements on scale growth in high-temperature oxidation of pure nickel, iron, cobalt, and copper, J. Electrochem. Soc. 141 (1994) 1905, http://dx.doi.org/10.1149/1.2055025.
[38] B.A. Pint, Optimization of reactive-element additions to improve oxidation performance of alumina-forming alloys, J. Am. Ceram. Soc. 86 (2003) 686–695, http://dx.doi.org/10.1111/j.1151-2916.2003.tb03358.x.
[39] D. Naumenko, B.A. Pint, W.J. Quadakkers, Current thoughts on reactive element effects in alumina-forming systems: in memory of John Stringer, Oxid. Met. 86 (2016) 1–43, http://dx.doi.org/10.1007/s11085-016-9625-0.
[40] A.U. Munawar, U. Schulz, M. Shahid, Microstructure and lifetime of EB-PVD TBCs with Hf-doped bond coat and Gd-zirconate ceramic top coat on CMSX-4 substrates, Surf. Coat. Technol. 299 (2016) 104–112, http://dx.doi.org/10.1016/j.surfcoat.2016.05.005.
[41] B.A. Pint, J.A. Haynes, Y. Zhang, Effect of superalloy substrate and bond coating on TBC lifetime, Surf. Coat. Technol. 205 (2010) 1236–1240, http://dx.doi.org/10.1016/j.surfcoat.2010.08.154.
[42] H. Guo, D. Li, L. Zheng, S. Gong, H. Xu, Effect of co-doping of two reactive elements on alumina scale growth of β-NiAl at 1200 °C, Corros. Sci. 88 (2014) 197–208, http://dx.doi.org/10.1016/j.corsci.2014.07.036.
[43] K. Yan, H. Guo, S. Gong, High-temperature oxidation behavior of β-NiAl with various reactive element dopants in dry and humid atmospheres, Corros. Sci. 83 (2014) 335–342, http://dx.doi.org/10.1016/j.corsci.2014.02.033.
[44] X.Q. Cao, R. Vassen, D. Stoever, Ceramic materials for thermal barrier coatings, J. Eur. Ceram. Soc. 24 (2004) 1–10 http://www.sciencedirect.com/science/article/B6TX0-48JSKKW-6/2/0ba27c573f9d4eebe5aa8bb1e6aa2a72.
[45] R. Vassen, M.O. Jarligo, T. Steinke, D.E. Mack, D. Stoever, Overview on advanced thermal barrier coatings, Surf. Coat. Technol. 205 (2010) 938–942, http://dx.doi.org/10.1016/j.surfcoat.2010.08.151.
[46] B. Ning, M. Shamsuzzoha, M.L. Weaver, Microstructure and properties of DC magnetron sputtered NiAl-Hf coatings, Surf. Coat. Technol. 179 (2004) 201–209, http://dx.doi.org/10.1016/S0257-8972(03)00870-3.
[47] M. Bestor, A. Brown, R. Martens, B. Ning, M. Miller, M. Weaver, Microstructures and properties of dispersion strengthened NiAl bond coats, Microsc. Microanal. 13 (2007) 2006–2007, http://dx.doi.org/10.1017/S1431927607071802.
[48] M.A. Bestor, Investigation of the Effect of Hafnium and Chromium Additions on the Microstructures and Short-Term Oxidation Properties of Dc Magnetron Sputtered β-Nial Bond Coats Deposited on Ni-Based Superalloys, (2010).
[49] L. Wei, H. Peng, F. Jia, L. Zheng, S. Gong, H. Guo, Cyclic oxidation behavior of Hf/Zr co-doped EB-PVD β-NiAl coatings at 1200 °C, Surf. Coat. Technol. 276 (2015) 721–725, http://dx.doi.org/10.1016/j.surfcoat.2015.05.039.
[50] A. Lange, R. Braun, M. Heilmaier, Oxidation behavior of magnetron sputtered double layer coatings containing molybdenum, silicon and boron, Intermetallics 48 (2014) 19–27, http://dx.doi.org/10.1016/j.intermet.2013.09.007.
[51] K.S. Murphy, K.L. More, M.J. Lance, As-deposited mixed zone in thermally grown oxide beneath a thermal barrier coating, Surf. Coat. Technol. 146–147 (2001) 152–161, http://dx.doi.org/10.1016/S0257-8972(01)01371-8.
[52] W.J. Quadakkers, V. Shemet, D. Sebold, R. Anton, E. Wessel, L. Singheiser, Oxidation characteristics of a platinized MCrAlY bond coat for TBC systems during cyclic oxidation at 1000 °C, Surf. Coat. Technol. 199 (2005) 77–82, http://dx.doi.org/10.1016/j.surfcoat.2004.11.038.
[53] A.L. Bement, C.T. Liu, A. Schaffhauser, N.M.A.B. (NAS-N.W. DC.), Structural Uses for Ductile Ordered Alloys. Report of the Committee on Application Potential for Ductile Ordered Alloys, (1984).
[54] G.J. Santoro, D.L. Deadmore, C.E. Lowell, Oxidation of Alloys in Nickel-Aluminum System With Third Element Additions of Chromium, Silicon and Titanium at 1100 °C, (1971).
[55] J.A. Thornton, Influence of apparatus geometry and deposition conditions on the structure and topography of thick sputtered coatings, J. Vac. Sci. Technol. 11 (1974) 666, http://dx.doi.org/10.1116/1.1312732.
[56] M.S.A. Karunaratne, S. Kyaw, A. Jones, R. Morrell, R.C. Thomson, Modelling the coefficient of thermal expansion in Ni-based superalloys and bond coatings, J. Mater. Sci. 51 (2016) 1–14, http://dx.doi.org/10.1007/s10853-015-9554-3.
[57] P.V.N. Rao, K.S. Murthy, S.V.N. Naidu, High temperature thermal expansion characteristics of Ni3Al alloys, J. Alloys Compd. 190 (1993) L33–L35.
[58] V. Teixeira, Residual Stress and Cracking in Thin PVD Coatings, 64 (2002), pp. 393–399.
[59] B. Sundman, J. Ågren, A regular solution model for phases with several components and sublattices, suitable for computer applications, J. Phys. Chem. Solids 42 (1981) 297–301, http://dx.doi.org/10.1016/0022-3697(81)90144-X.
[60] N. Saunders, Phase diagram calculations for Ni-based superalloys, in: R.D. Kissinger, D.J. Deye, D.L. Anton, A.D. Cetel, M.V. Nathal, T.M. Pollock, D.A. Woodford (Eds.), Superalloys, 1996, pp. 101–110.
[61] C. Jiang, Site preference of transition-metal elements in B2 NiAl: a comprehensive study, Acta Mater. 55 (2007) 4799–4806, http://dx.doi.org/10.1016/j.actamat.2007.04.049.
[62] B. Gleeson, W.H. Cheung, D.J. Young, Cyclic oxidation behaviour of two-phase Ni–Cr–Al at 1100 °C, Corros. Sci. 35 (1993) 923–928.
[63] V.K. Tolpygo, D.R. Clarke, On the rumpling mechanism in nickel-aluminide coatings part I: an experimental assessment, Acta Mater. 52 (2004) 5115–5127, http://dx.doi.org/10.1016/j.actamat.2004.07.019.
[64] A.U. Munawar, U. Schulz, G. Cerri, H. Lau, Microstructure and cyclic lifetime of Gd and Dy-containing EB-PVD TBCs deposited as single and double-layer on various bond coats, Surf. Coat. Technol. 245 (2014) 92–101, http://dx.doi.org/10.1016/j.surfcoat.2014.02.047.
[65] S. Kitaoka, Mass transfer in polycrystalline alumina under oxygen potential gradients at high temperatures, J. Ceram. Soc. Japan 124 (2016) 1100–1109, http://dx.doi.org/10.2109/jcersj2.16140.